Materials & Design 224 (2022) 111349

Contents lists available at ScienceDirect

Materials & Design

journal homepage: www.elsevier.com/locate/matdes

Design and fabrication of micro and nano surface structures for enhancing metal–polymer adhesion using femtosecond laser treatment

Masaki Omiya *, Ayumi Nakajima, Jiwang Yan

Department of Mechanical Engineering, Keio University, 3-14-1, Hiyoshi, Kohoku-ku, Yokohama, Kanagawa 223-8522, Japan

HIGHLIGHTS

- Fracture mechanics models to derive a surface profile that enhances the adhesion strength are proposed.
- Microgrooves with a laser-induced periodic surface structure (LIPSS) were successfully fabricated on a copper surface.
- The enhancement of adhesion strength was confirmed by both numerical simulations and button shear tests.
- The study revealed the LIPSSs formations on microgrooves suppress shear deformation and interface crack propagation.

GRAPHICAL ABSTRACT

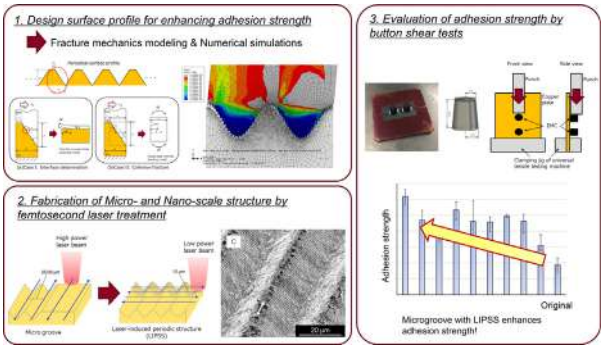

ARTICLE INFO

Article history:
Received 9 August 2022
Revised 24 October 2022
Accepted 4 November 2022
Available online 5 November 2022

Keywords:
Micro and nano surface structures
Surface treatment
Adhesion strength
Laser
LIPSS
Copper
Electronic packaging

ABSTRACT

This study investigated the effects of micro- and nanostructures on the adhesion strength between copper and an encapsulating mold compound (EMC). The shape of the microgrooves was designed based on fracture mechanics theory, and the effect of laser-induced periodic structure surface (LIPSS) formation on the microgroove was investigated using numerical simulations. The designed surface profiles were fabricated using femtosecond laser treatments, and the adhesion strength between copper and the EMC was evaluated. The results show that deep microgrooves improved the adhesion strength owing to the anchor effect. However, the aspect ratio between the pitch and depth of the microgroove had a limitation in enhancing the adhesion strength. The formation of LIPSSs on the mountaintop of the microgroove was very effective; however, an LIPSS on the valley of the microgroove was ineffective. Numerical analyses revealed that LIPSSs suppressed the shear deformation of the EMC and worked as resistance to interface delamination. Based on the findings obtained in this study, combining micro- and nano-scale surface structure formation with femtosecond laser treatments is an effective and eco-friendly method for improving adhesion strength.

1. Introduction

Along with the rapid integration of semiconductors for achieving higher speed and lower energy consumption, new multi-layer, miniaturized, and low-profile electronic package technologies have been developed. In addition, with the rapid development of hybrid electric and purely electric vehicles, SiC and GaN power devices have emerged, which work at higher temperatures than conventional silicon-based technologies, bringing new issues such as the introduction of heat-resistant materials or thermal management in the system [1–4]. Furthermore, owing to the strong enforcement

* Corresponding author.
E-mail address: oomiya@mech.keio.ac.jp (M. Omiya).

https://doi.org/10.1016/j.matdes.2022.111349
0264-1275/

of the mandate for reducing CO_2 emissions, electrification is spreading not only to the automobile industry but also to the aircraft industry [5], and highly reliable semiconductor products will be required in the future.

Electric packages are composed of chips, lead frames, and encapsulating mold compounds (EMCs), which have different mechanical properties, such as elastic moduli and thermal expansion coefficients. During the reflow soldering process or usage of these products, delamination at the interface between different materials is likely to occur owing to thermal stress. In particular, owing to the weak bonds of the intermolecular forces, the interfaces between the metal lead frames and the EMCs have a low interfacial strength; therefore, it is necessary to improve the adhesion between the lead frames and the EMCs to suppress delamination and prevent package failures [6–12].

The fundamental principles of adhesion can be classified into chemical bonds, physical interactions such as van der Waals forces, and mechanical locking such as anchor effects. Surface structures change the true contact area and affect the physical interactions between adherents. Usually, surface energy is the material property representing the strength of physical interactions. The surface energy is measured by dropping a water droplet on the surface of the material and measuring the contact angle to evaluate wettability. Subsequently, the contact angle is related to the surface energy via the Young–Dupre equation. Wenzel [13] and Cassie–Baxter [14] revealed that the contact angle, that is, the surface energy, depends on surface roughness. After their pioneering work, many studies on creating superhydrophobic or super-hydrophilic surfaces were conducted [15–23]. However, most of these studies deal with the phenomena occurring at the solid–liquid interface [24–26].

Mechanical locking is generated by bonding between solids, and when another material enters the rough surface of one material, a strong bonding force is created [27–30]. Methods for forming irregularities on metal surfaces include chemical etching [31], surface oxidation [32], and groove formation by laser treatment [33]. Recently, research on the formation of surface irregularities using biomimetics has been actively conducted [34–35].

Laser treatment has many industrial merits, including partial treatment of the surface of the material, reduced steps and processing time, and eco-friendliness. Furthermore, in recent years, the technique of forming a periodic nanostructure, that is, laser-induced periodic surface structure (LIPSS), on a metal surface by laser processing has been studied [36–39]. The advantage of LIPSS treatment is that it can enhance the adhesion strength by increasing the surface area and roughness, increasing the true contact area and the mechanical locking sites more than in microgrooves treatment alone. The disadvantage is that an additional process is required for LIPSS formation after developing microgrooves. Examples of applying the composite structure of microgrooves and LIPSSs to copper materials are few. In addition, little research has been conducted on the contribution of such composite processing of microgrooves and LIPSSs to the improvement of adhesion strength. Moreover, the surface profile has almost no design guidelines to enhance adhesion strength using the anchor effect.

Therefore, this study aims to derive a design guideline for the surface profile of microgrooves to enhance the adhesion strength. Furthermore, this surface profile is demonstrated by fabricating microgrooves and LIPSSs on a copper surface using a femtosecond laser treatment. Moreover, to verify the enhancement in adhesion strength, EMCs were formed on the surface-treated copper plate, and the shear strength was measured. Lastly, the mechanism of adhesion enhancement with microgrooves and LIPSSs was discussed based on finite element simulations.

The remainder of this paper is organized as follows. In Section 2, a theoretical model based on fracture mechanics is proposed to design the surface profile of the microgroove to enhance adhesion strength. In Section 3, in addition to the surface profile of the microgroove, the effect of LIPSS formation is investigated using numerical analyses, and the surface profiles used in the experiments are determined. In Section 4, composite surface structures of microgrooves and LIPSSs on copper plates are fabricated using femtosecond laser treatment. In Section 5, EMCs are formed on the surface-treated copper plates, the adhesion strength is evaluated by button shear tests, and the fracture mechanism is discussed according to surface morphology observations.

2. Design of surface profile based on fracture mechanics

2.1. Fracture mechanics modeling

Usually, the interface between a polymer and metal fails as a combination of interfacial and cohesive failures. Yao and Qu [40] proposed a mechanical model based on fracture mechanics to describe the failure modes of metal–polymer interfaces under tensile loading. However, in electronic packages, shear loading is dominant because of the difference in thermal expansion during molding, reflow processes, and service conditions. Therefore, in this section, considering the interfacial and cohesive failure of the metal–polymer interface crack under shear loading, the design diagram to select the optimum shape with high adhesive strength is derived.

The interface profile of the copper–EMC with a depth (d), half-wavelength of the pitch (λ), and flat top surface length (s) is considered, as shown in Fig. 1. Subsequently, two failure modes are considered, and the maximum shear stress is derived for each case.

Case I: Interface delamination on copper/EMC interface

Assuming that part of the interface has already separated, as shown in Fig. 1(a), the critical shear stress at which the interface crack begins to propagate on the interface is derived. The interface crack model is introduced, in which the equivalent moment is applied to a thin film on a semi-infinite plate, as shown in Fig. 1 (a). From dimensional analysis, the equivalent moment acting on a unit thickness is described as

$$M = \alpha \tau_0 \lambda d, \tag{1}$$

where α is a coefficient. In addition, by introducing geometrical parameters γ and $h = \gamma d$, the energy release rate of the interface crack, G_i, is derived as [41]:

$$G_i = \frac{1}{2\bar{E}_{\mathrm{emc}} h} \frac{12M^2}{h^2} = \frac{6M^2}{\bar{E}_{\mathrm{emc}} h^3}, \tag{2}$$

$$\bar{E}_{\mathrm{emc}} = \frac{E_{\mathrm{emc}}}{1-\nu_{\mathrm{emc}}}, \tag{3}$$

where E_{emc} and ν_{emc} are the Young's modulus and Poisson's ratio of the EMC, respectively. If the interface crack begins to propagate under $G_i = G_i^c$, the normalized critical shear stress is expressed as follows:

$$\frac{\tau_0^c}{\alpha' \bar{E}_{\mathrm{emc}}} = \frac{\sqrt{d}}{\lambda} \sqrt{\frac{G_i^c}{\bar{E}_{\mathrm{emc}}}}, \tag{4}$$

where $\alpha' = \sqrt{6\alpha^2/\gamma^3}$.

Case II: Cohesive fracture in EMC

Subsequently, assuming that part of the interface has already separated, as shown in Fig. 1(b), the critical shear stress in the case where the interface crack kinks and propagates into the EMC is derived. The kinked crack length, δ, is introduced, and the single-edge notched specimen under the applied moment of Eq. (1) is considered. The stress intensity factor of this model is described as [42]

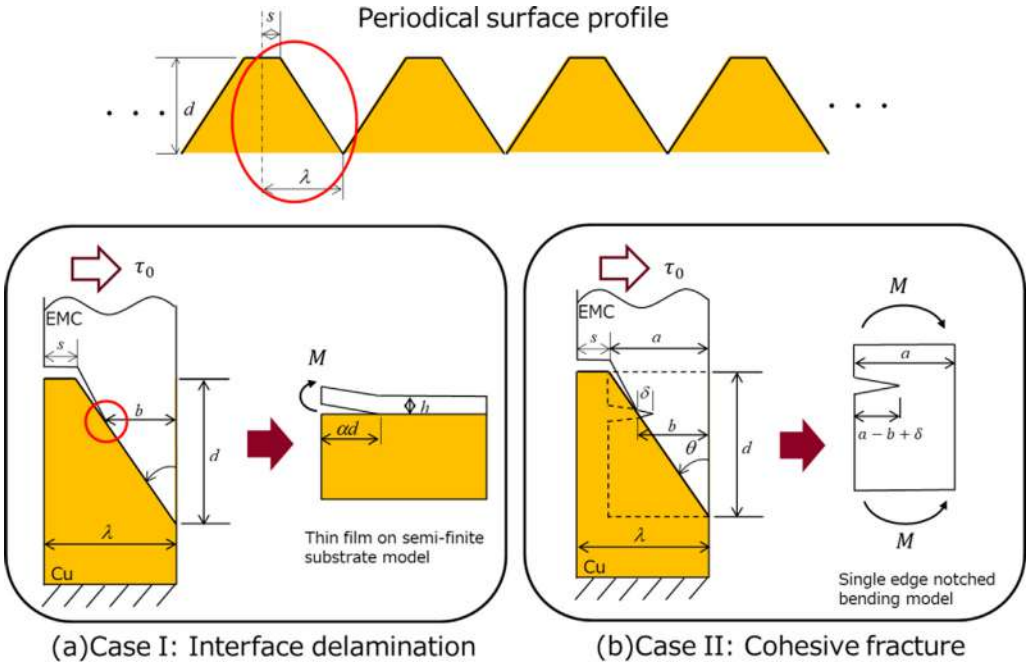

Fig. 1. Fracture mechanics models for interface delamination and cohesive fracture.

$$K_{\mathrm{I}} = \frac{M}{a^{\frac{3}{2}}} \frac{6\sqrt{2\tan\frac{\pi(a-b+\delta)}{2a}}}{\cos\frac{\pi(a-b+\delta)}{2a}} \left[0.923 + 0.199\left\{1 - \sin\frac{\pi(a-b+\delta)}{2a}\right\}^4\right] \tag{5}$$

When the critical condition as $\delta \to 0$ is considered, the stress intensity factor at which the crack begins to propagate is

$$K_{\mathrm{I}} = \frac{M}{a^{\frac{3}{2}}} \frac{6\sqrt{2\tan\frac{\pi(1-\omega)}{2}}}{\cos\frac{\pi(1-\omega)}{2}} \left[0.923 + 0.199\left\{1 - \sin\frac{\pi(1-\omega)}{2}\right\}^4\right] = \frac{M}{a^{\frac{3}{2}}} f(1-\omega), \tag{6}$$

where f is a function of $\omega = b/a (0 < \omega < 1)$. Subsequently, the energy release rate, G_{emc}, is derived as

$$G_{\mathrm{emc}} = \frac{K_{\mathrm{I}}^2}{\bar{E}_{\mathrm{emc}}} = \frac{\tau_0^2 \lambda^2 \alpha^2 d^2}{\bar{E}_{\mathrm{emc}}(\lambda - s)^3} \{f(1-\omega)\}^2 \tag{7}$$

The crack begins to propagate when the energy release rate reaches the fracture toughness of the EMC, $G_{\mathrm{emc}} = G_{\mathrm{emc}}^c$. The normalized critical shear stress is described as

$$\frac{\alpha \tau_0^c}{\bar{E}_{\mathrm{emc}}} = \frac{\sqrt{\lambda}}{d} \frac{(1-\omega\prime)^{\frac{3}{2}}}{f(1-\omega)} \sqrt{\frac{G_{\mathrm{emc}}^c}{\bar{E}_{\mathrm{emc}}}}, \tag{8}$$

where $\omega\prime = s/\lambda (0 < \omega\prime < 1)$.

2.2. Design guideline for periodical surface profile

If the half-wavelength, λ, and the flat top surface length, $s (0 \le s \le \lambda)$, are fixed, the critical shear stress of the interfacial fracture in Eq. (4) monotonically increases with depth (d), whereas the critical shear stress of the cohesive fracture in Eq. (8) monotonically decreases with depth (d). For example, considering the material parameters in Table 1 and assuming $G_i^c = 11.5\ \mathrm{J/m^2}$[43], $G_{\mathrm{emc}}^c = 7550\ \mathrm{J/m^2}$[40], and $\omega = \omega\prime = 0.5$, the normalized shear stresses can be obtained as shown in Fig. 2. The normalized shear stresses of the interfacial and cohesive fractures exhibit a trade-off relationship. The maximum normalized shear stress is obtained when the following equation is satisfied:

$$\frac{\sqrt{d}}{\lambda} \sqrt{\bar{E}_{\mathrm{emc}} G_i^c} = \frac{\sqrt{\lambda}}{d} \frac{(1-\omega\prime)^{\frac{3}{2}}}{f(1-\omega)} \sqrt{\bar{E}_{\mathrm{emc}} G_{\mathrm{emc}}^c} \tag{9}$$

Table 1
Material properties.

	EMC (Encapsulating mold compound)	Copper
Young's modulus (GPa)	25	118
Poisson's ratio	0.3	0.3
Yield stress (MPa)	75	-
Damage initiation strain	0.04	-
Fracture energy ($\mathrm{J/m^2}$)	15	-
Interfacial stiffness, K_{n} (GPa)	25	
Interfacial maximum traction, $t_{\max}$ (MPa)	25	
Interfacial fracture energy, G_i^c ($\mathrm{J/m^2}$)	11.5	

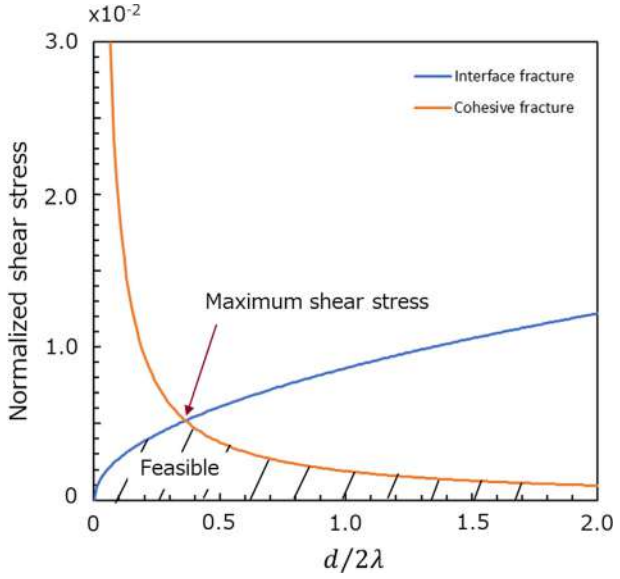

Fig. 2. Fracture boundary depending on the aspect ratio between the pitch and the depth of the microgroove.

Subsequently, the optimum aspect ratio between the pitch, 2 λ, and the profile depth, d, is determined as

$$\frac{d}{2\lambda} = \frac{1-\omega'}{\{f(1-\omega)\}^{2/3}} \left(\frac{G^c_{emc}}{G^c_i}\right)^{1/3}, \quad (10)$$

where $\omega(=b/a)$ is a coefficient that relates to the delamination length, and $\omega'(=s/\lambda)$ is the coefficient that relates to the length of the flat surface of the mountaintop of the microgroove. In Fig. 2, the optimum normalized shear stress is obtained at an aspect ratio of $d/2\lambda = 0.437$. Then, the failure mode of the copper–EMC interface is expected to be

$$\begin{aligned} &\frac{d}{2\lambda} < 0.437 \quad \text{(Interfacial fracture between Cu and EMC)} \\ &\frac{d}{2\lambda} > 0.437 \quad \text{(Cohesive fracture in EMC)} \end{aligned} \quad (11)$$

The effects of the delamination and flat mountaintop surface lengths are shown in Fig. 3. The critical shear stress tends to increase as $\omega' \to 0 (s \to 0)$ and $\omega \to 1 (b \to 0)$. Therefore, it is suggested that the surface profile with higher adhesive strength has a triangular shape with a larger aspect ratio.

It should be noted that this estimation assumes that copper and EMC are elastic and that it is impossible to predict the critical shear force quantitatively because of plastic deformation in the EMC. However, even in elastic estimation, this is a useful guideline for designing a surface profile with an optimum aspect ratio that has a higher adhesion strength. The effect of plastic deformation in the EMC is discussed in the next section based on finite element analyses.

3. Numerical simulation

3.1. Numerical model

This section presents numerical simulations carried out to investigate the effects of the microgroove profile and LIPSS formation on adhesive strength. A two-dimensional unit cell model with a periodic surface profile was developed using the ABAQUS/CAE 2019 software with a Python script, as shown in Fig. 4. The model size was deduced to be sufficiently large to prevent stress interaction between the top and the interface. The material properties and interface parameters used in the numerical simulations are presented in Table 1. Copper was assumed to be an elastic material. The EMC was assumed to be an elastic–plastic material. The bottom edge of the model was fixed, and the left and right edges were set as periodic boundary conditions in the horizontal direction using the *EQUATION command in the ABAQUS software [44,45]. The enforced horizontal displacement was applied to the top of the model, and the shear stress was calculated using the total reaction force on the top edge. At the copper–EMC interface, isotropic cohesive contact surface interaction, which has a linear traction–separation relation with damage initiation and evolution, was introduced. Damage was assumed to initiate when a quadratic interaction function had a value of one, and damage evolution was based on a power-law fracture criterion, which describes the failure under mixed-mode conditions as a power law interaction of the energies required to cause failure in the individual modes [44]. Four-node plane strain finite elements were used, and through a convergence check for element size, the minimum element size was deduced to be approximately 6.5×10^{-2} μm. The total number of elements and nodes were approximately 22,600 and 23,600, respectively.

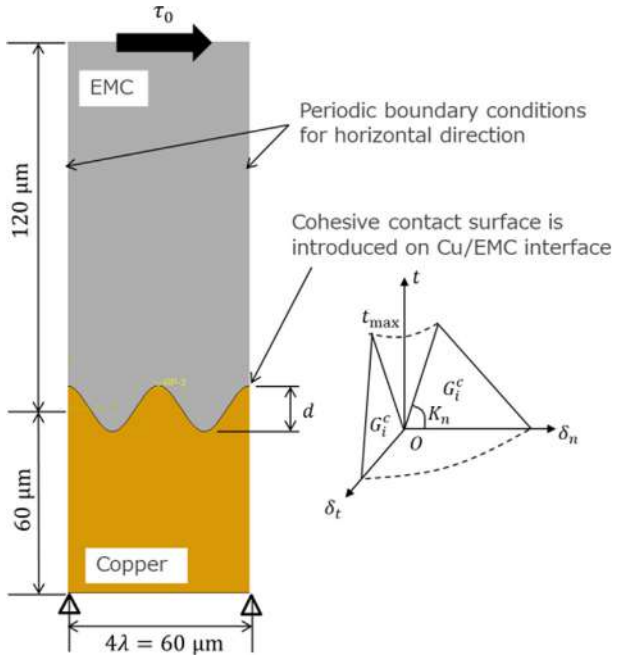

Fig. 4. Unit cell model with two concave microgrooves for numerical simulation.

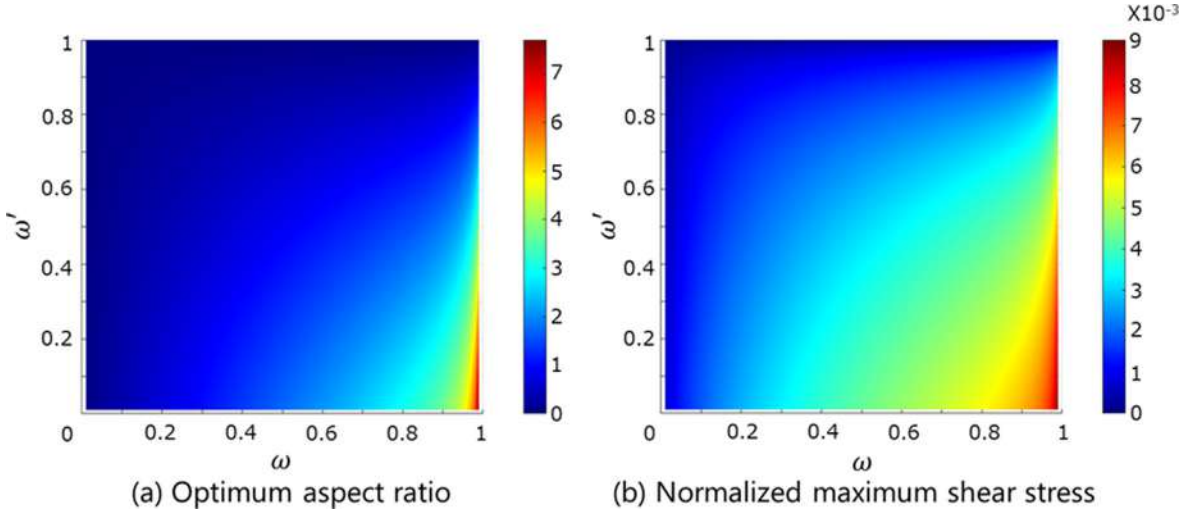

Fig. 3. Effect of delamination and flat mountain top lengths on optimum aspect ratios and normalized critical shear stresses.

For the surface profile of the microgrooves, sine curves with a wavelength of $2\lambda = 30$ μm and heights of d = 0, 7.5, 15, 22.5, 37.5 μm were introduced to mimic the laser treatment. In our fabrication process, the size of LIPSSs was 0.81 ± 0.03 μm on the flat surface and 1.87 ± 0.10μm on the slope. The size of LIPSSs depends on the condition of the interfering laser beam. To compare under the same condition, the LIPSS profiles were assumed to be sine curves with a wavelength of 1 μm and a height of 1 μm and were superposed on the microgroove wave. The locations where LIPSSs were formed changed in the following four patterns: on the entire surface of the microgrooves, only on the mountaintops, only on the valleys, and only on the slopes.

3.2. Numerical results

Fig. 5 shows the rate of increase in the adhesion strength of only the microgroove models when the aspect ratio, $d/2\lambda$, is changed. The results show that the adhesion strength increased with the aspect ratio, and the adhesion strengths for aspect ratios above $d/2\lambda = 0.5$ were almost the same for the microgroove models without LIPSSs. In addition, it was found that the aspect ratio of $d/2\lambda = 0.5$ was close to 0.437, which had the maximum shear stress in the theoretical prediction. In the theoretical model, cohesive fracture due to crack propagation in the EMC was considered under the assumption that the EMC was an elastic material and that the shear strength decreased beyond the critical aspect ratio, as shown in Fig. 2. However, when the EMC was considered as an elastic–plastic material, shear failure due to plastic deformation in the EMC occurred, and the shear strength maintained the same value over the critical aspect ratio. This implied that the theoretical model could be applied to determine the critical aspect ratio, and there was a limitation in the adhesion strength. Therefore, creating a deep and narrow groove is not always effective in improving adhesion strength.

Subsequently, the effects of LIPSS formation on the adhesion strength are compared for aspect ratios of $d/2\lambda = 0.5, 0.75,$ and 1.25 in Fig. 6. From these figures, it can be seen that the models with LIPSSs on the valleys and slopes at $d/2\lambda = 0.5, 0.75$ have lower adhesion strength than the models for which only microgrooves were considered. LIPSSs on the entire surface and mountaintops resulted in a larger adhesion strength than that in the model for which only microgrooves were considered. This result indicates that increasing the surface roughness does not always enhance the adhesion strength and that the location of LIPSS formation is an important design factor for enhancing the adhesion strength.

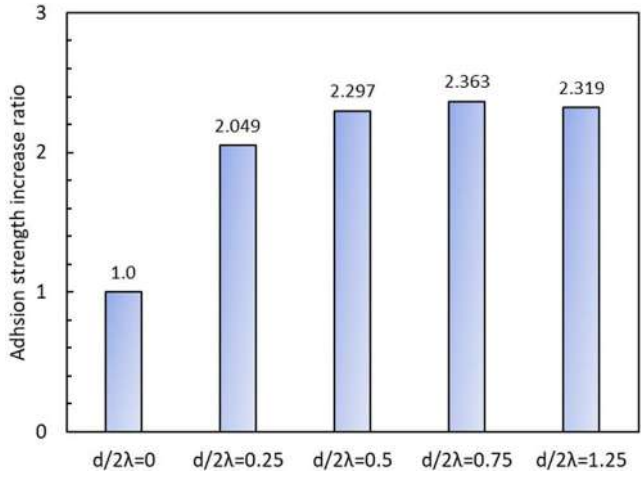

Fig. 5. Adhesion strength increase ratio for several aspect ratios of microgrooves without LIPSSs.

Fig. 7 shows the distributions of equivalent plastic strains of the model with LIPSS formation on the entire surface of the microgroove and the model with LIPSS formation on the valley at $d/2\lambda = 0.5$. Damage occurs in the region where the equivalent plastic strain is greater than 0.04, which is gray in the EMC. In the case of the LIPSS formation on the entire surface, as shown in Fig. 7(a), although delamination of the copper–EMC interface occurs around the mountaintops, LIPSS effectively suppresses the expansion of the delamination and shear deformation of the EMC. On the other hand, in the case of the LIPSS formed on the valleys, as shown in Fig. 7(b), delamination of the copper–EMC occurs around the mountaintop, and the damaged region is connected from the mountaintops due to shear deformation of the EMC, resulting in a shear fracture in the EMC. In this case, LIPSS does not effectively suppress delamination of the copper–EMC. LIPSS suppresses the expansion of copper–EMC delamination and prevents EMC failure that occurs due to the connection of plastic strains concentrated around the mountaintops. Therefore, to increase the adhesion strength, it is more effective to form LIPSS on the entire surface or mountaintops than on valleys.

Based on the discussion above, candidates for surface profiles with higher adhesion strengths are summarized in Table 2. In the following sections, the candidate surface profiles are fabricated using femtosecond laser treatment, and the adhesion strength is evaluated using button shear tests.

4. Fabrication of microgroove and LIPSS on copper surface

This section presents microgrooves and LIPSSs fabricated on a copper surface using femtosecond laser treatment. The Yb:KGW femtosecond pulse laser system (PHAROS-08-600-PP, Light Conversion) was used in this study [46]. The laser treatment conditions are summarized in Table 3. First, microgrooves were formed by irradiation with a high energy density and wide pitch, followed by the formation of LIPSS on the microgrooves by irradiation with a low energy density and narrow pitch.

Table 4 summarizes the dimensions of the fabricated specimens, and Fig. 8 shows the specimen surface obtained by scanning electron microscope (SEM). Specimens A and B had LIPSSs on the top of the microgroove. Specimen C had LIPSSs on the entire surface, and Specimen D had LIPSSs on both the top and the valley of the microgroove. Specimens E and F had LIPSSs in the valley of the microgroove. By comparing specimens A, B, and C, it can be seen that LIPSSs did not form on the slope as the aspect ratio increased. This is because the area where one pulse is irradiated increases owing to the inclination, and the energy density decreases; therefore, the energy density required for LIPSS formation is not satisfied. By comparing specimens D and F, it can be seen that LIPSSs were formed not only in the valley but also on the mountaintop due to the widening of the pitch. This is because the unprocessed surface remained on the mountaintop when the microgroove was formed owing to the expansion of the pitch, and LIPSSs were formed in the unprocessed part by the second irradiation. By comparing specimens A to C with specimens E and F, it can be seen that the LIPSS formation position changes depending on the directions of the microgroove and LIPSS. This is because the interference state of the laser beam changes depending on the inclination direction of the microgroove slope with respect to the polarization direction. The LIPSS is thought to be caused by interference between the incident light and surface electromagnetic waves, and many previous studies have shown that it is formed perpendicular to the polarization direction [36,37]. There-

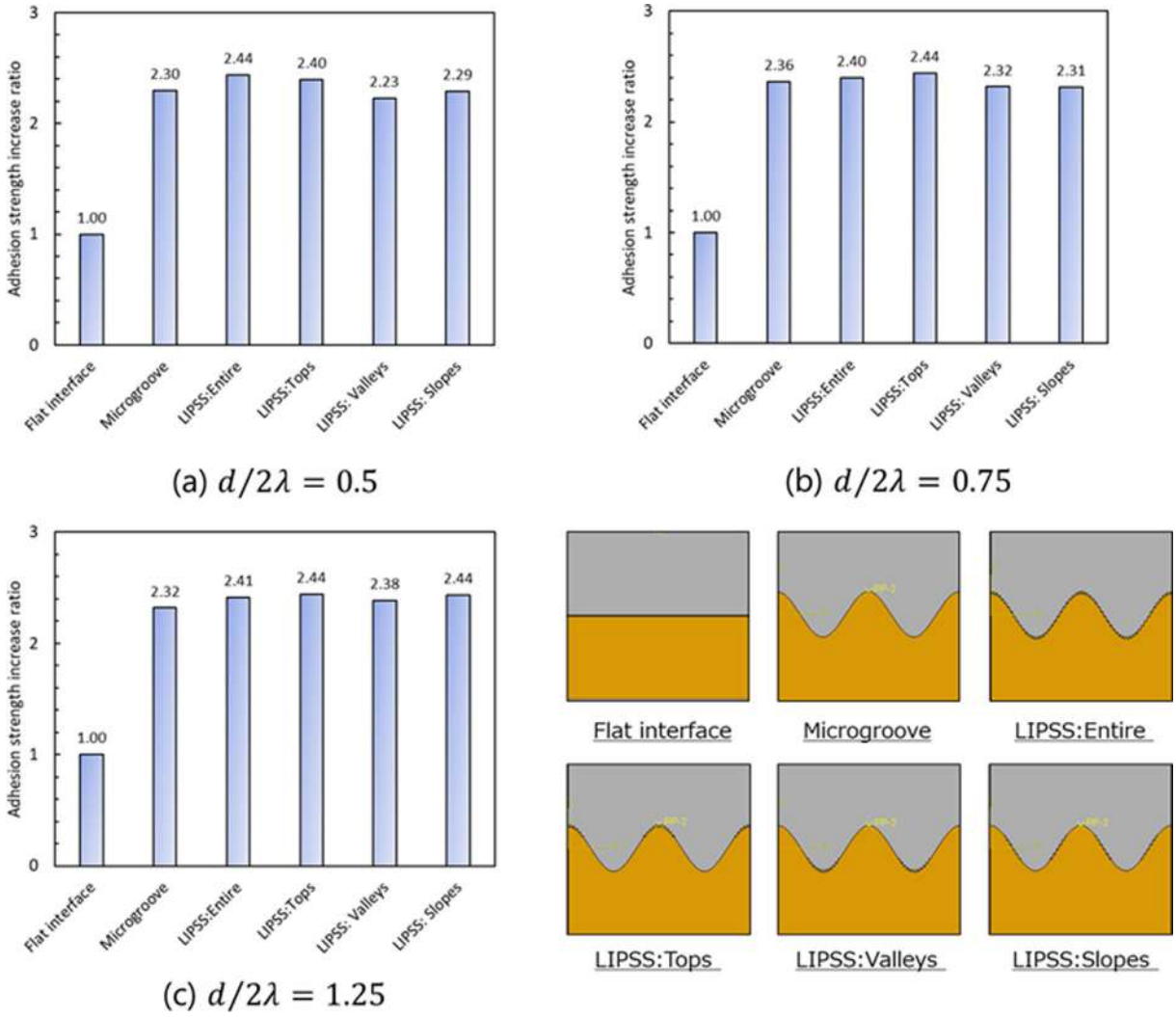

Fig. 6. Adhesion strength increase ratio for microgrooves with LIPSSs formation.

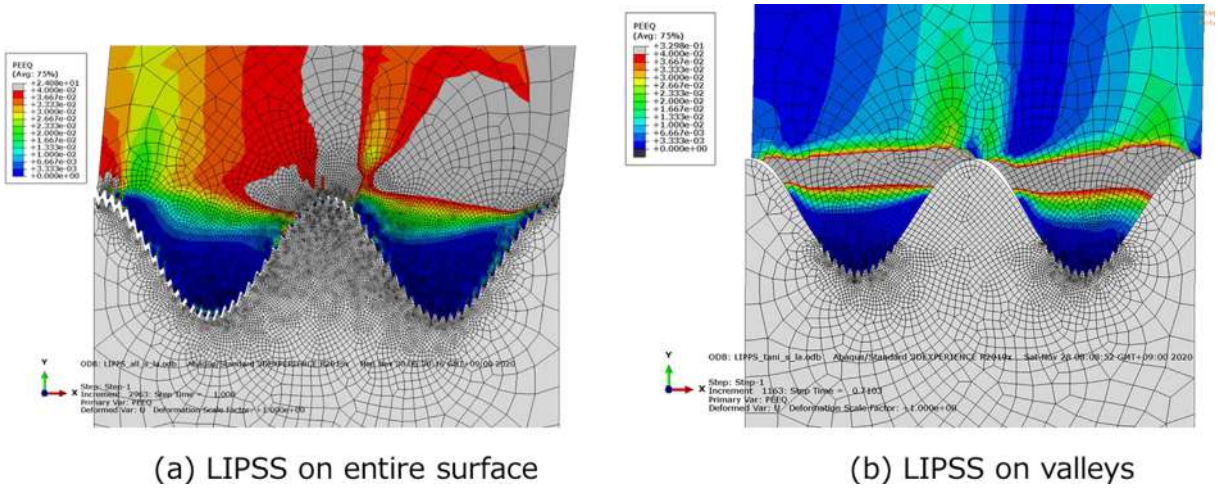

Fig. 7. Equivalent plastic strain distribution just before failure.

fore, when the microgroove and LIPSS were parallel, the slope was inclined in the polarization direction, and LIPSS formation was limited on the slope. However, when the microgroove and LIPSS were vertical, the slope was not inclined in the polarization direction. Then, LIPSS formation was evident on the slope when the aspect ratio was small.

Table 2
Candidates for surface profile and LIPSS position.

LIPSS place on Cu / Aspect ratio	Adhesion strength increase ratio
Entire surface/0.5	2.44
Top /0.75	2.44
Top /1.25	2.44

Table 3
Laser treatment conditions.

	Microgroove	LIPSS
Wavelength [nm]	1030	
Pulse interval [fs]	256	
Laser spot diameter [μm]	20	
Repeat frequency [kHz]	100	
Energy density [J/cm^2]	4.0, 4.5	0.5
Scan rate [mm/s]	9.5, 14.4, 30	50
Irradiation pitch [μm]	25, 30	10

Table 4
Dimension and LIPSS condition of fabricated specimens.

Specimen	Microgroove		LIPSS		Aspect ratio $d/2\lambda$
	2λ[μm]	d[μm]		Place	
A	30	22	○	Top	0.73
B	30	15	○	Top	0.5
C	30	7	○	Entire	0.23
D	30	14	○	Top + Valley	0.47
E	25	17	○	Valley	0.68
F	25	13	○	Valley	0.52
G	25	11	×	-	0.44
H	25	10	×	-	0.4
I	-	-	○	Entire	≒0
J	-	-	×	-	≒0

5. Evaluation of adhesion strength by button shear tests

5.1. Experimental method

This section presents an evaluation by button shear tests of the adhesion strength of the fabricated copper–EMC (presented in the previous section) and a discussion of the effect of the surface profile on the adhesion strength. As shown in Table 4, there were four patterns of LIPSSs formation on the microgrooves: only on the mountaintops, only on the valleys, both on the mountaintops and valleys, and on the entire surface of the microgrooves. In addition, the aspect ratio, $d/2\lambda$, which is the ratio of the microgroove pitch, 2λ, to the microgroove depth, d, was used as an index to discuss the unevenness of the microgroove.

The button shear test is widely used in the electronics industry for the adhesion strength measurement of copper–EMC [43,47–49]. The specimen used for the button-shear test is shown in Fig. 9(a). A laser-processed copper plate after etching (Cu-Sn alloy (Sn: 0.1 to 0.15 %)), EMC (epoxy with 86 % silica filler), a mold for button shape, and a heat press machine were used, and the button shape of the EMC was molded on the laser-treated copper plates by hot pressing. As shown in Fig. 9(b), shear tests were performed using a universal tensile testing machine (EZ Graph, Shimadzu Co. ltd.) at a shear height of 0.2 mm and a shear rate of 0.017 mm/s. After the tests, the fracture surfaces were observed using SEM. Button shear tests were performed four times for each condition.

5.2. Experimental results

Fig. 10 shows typical load–displacement curves during button shear tests. In all cases, the load increased with displacement, and at the maximum load, the specimen suddenly fractured, that is, a shear fracture occurred between the copper and EMC. The effect of loading direction on microgroove direction can be observed from the initial deformation behavior. Applying a load parallel to the microgroove shows more compliant behavior, although the maximum load is not influenced by loading direction. The difference in the initial deformation behavior was small for the specimen with LIPSSs formation on the valley of microgrooves.

The average shear strength for each condition is shown in Fig. 11. The adhesion strength of specimen A, which has an aspect ratio of $d/2\lambda = 0.73$ and LIPSS on only the mountaintop, is the largest: the adhesion strength is approximately 3.3 times that of the original specimen without laser treatment. This tendency is consistent with the numerical results: the model with an LIPSS on the mountaintop showed one of the largest adhesion strengths, as shown in Fig. 6. Comparing specimens D (LIPSS: top and valley, $d/2\lambda = 0.47$) and G (only microgroove, $d/2\lambda = 0.44$), which have almost the same aspect ratios, the LIPSSs formation enhances the adhesion strength by approximately 7.3 % over that of the only microgroove structure.

Among specimens B, D, and F with an aspect ratio of approximately 0.5, specimen D with LIPSSs on both mountaintops and valleys has a larger adhesion strength than specimens B and F with LIPSSs on only the mountaintop or the valleys. Thus, LIPSSs on both mountaintops and valleys effectively enhances adhesion strength. Specimen E, which has a larger aspect ratio than specimen D and LIPSSs on the valleys, shows a lower adhesion strength than specimen D. LIPSSs on the valleys negatively affects the adhesion strength. Thus, the position where LIPSSs are formed is an important design factor for enhancing adhesion strength.

The fracture surfaces observed using SEM are shown in Fig. 12 for specimens A, B, D, and I.

During the button shear tests, the EMC fracture first occurred at the position where the punch was pushed owing to stress concentration. Subsequently, the crack progressed to the interface between the copper plate and the EMC. A shear fracture occurred when the remaining part of the EMC decreased. From Fig. 12(a), both cohesive fracture of the EMC and interfacial delamination of the copper–EMC on the top of the microgrooves can be observed for specimen A, although the EMC did not fill the valley of the microgrooves in some parts owing to the silica filler in the EMC. Because the average particle size of the silica filler was 25 μm and the pitch of the microgrooves was 30 μm, it is possible that the silica filler entered the microgroove and became an obstacle to epoxy resin flowing into the microgrooves. However, this case showed the largest adhesion strength, and both the large aspect ratio and LIPSS formation on the mountaintop effectively enhanced the adhesion strength. As shown in Fig. 12(b) and (c), cohesive fracture of the EMC occurred, and the microgrooves were filled with EMC on the fracture surface. This trend is the same as the numerical simulation results of EMC failure, as shown in Fig. 7. Moreover, in Fig. 12(c), the flat top surface of the microgroove with LIPSSs can be observed, and this works as a resistance to shear stress and results in the enhancement of the adhesion strength in specimen D. As shown in Fig. 12(d), not much EMC is left on the fracture surface of specimen I, which has only LIPSSs without microgrooves. This result indicates that the anchor effect did not work well for the specimen with a small aspect ratio, and the size of the microgroove was also an important design factor in enhancing the adhesion strength.

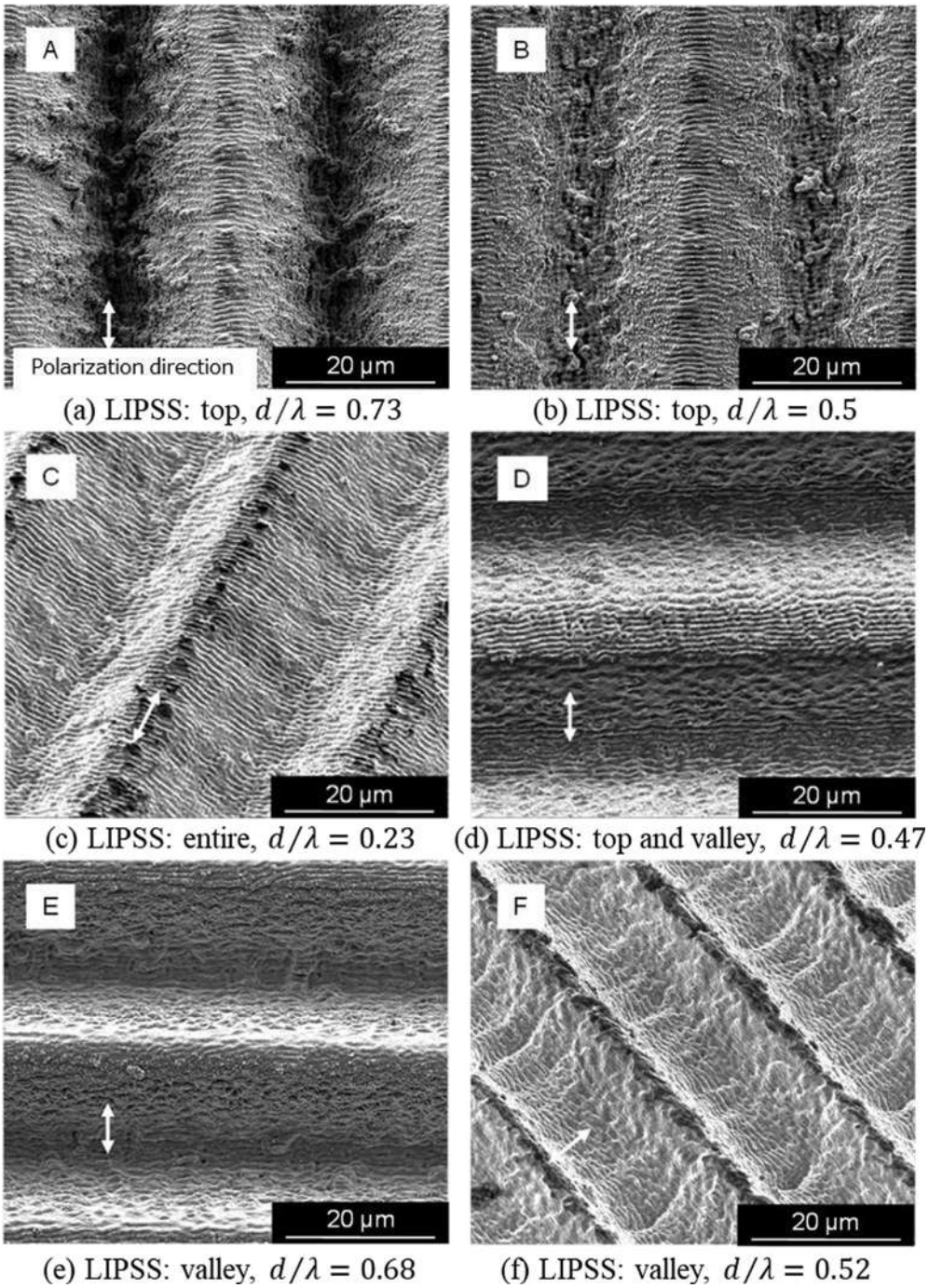

Fig. 8. SEM observation of the specimen surface.

6. Conclusion

To enhance the adhesion strength of the copper–EMC interface, the microgroove shape on the copper surface was designed using fracture mechanics theory, and the effect of LIPSS formation on the microgroove was investigated by finite element analyses. The designed surface profile was fabricated using femtosecond laser treatments, and the adhesion strength of the copper–EMC was evaluated using button shear tests. The results obtained are summarized as follows:

- By forming a deep microgroove, the adhesion between the copper and the EMC was improved owing to the anchor effect. However, it was found that there was a limitation in the aspect ratio between the pitch, 2λ, and depth, d, of the microgroove to enhance the adhesion strength. If the aspect ratio of the microgrooves exceeds the threshold value, which is the maximum limitation of the adhesion strength, the shear fracture in the EMC is dominant. In this study, the threshold was estimated using fracture mechanics theory to be $d/2\lambda = 0.437$.

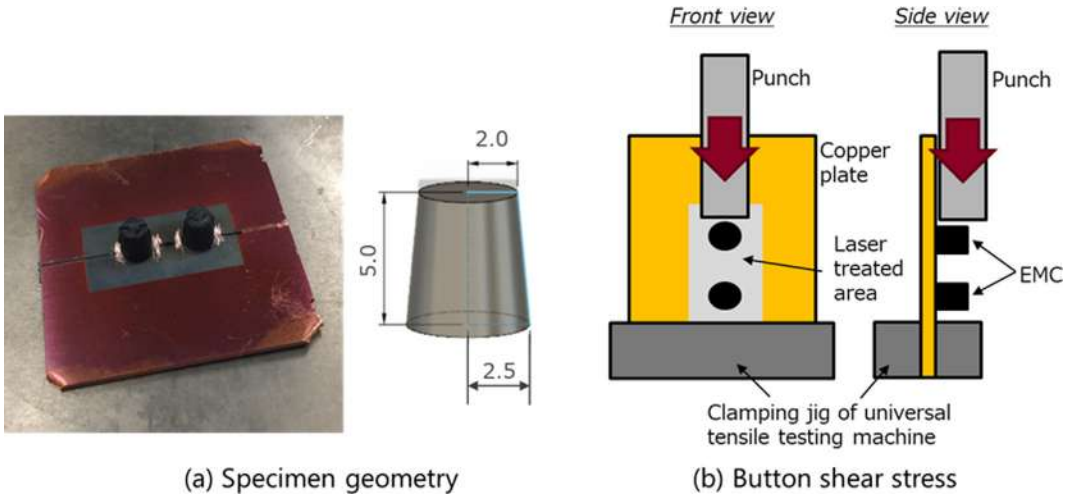

Fig. 9. Button shear test specimen and image of button shear test.

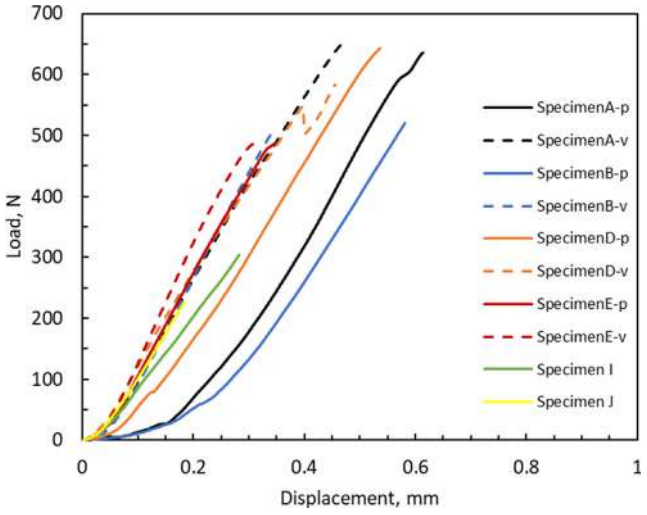

Fig. 10. Typical load–displacement curves during button shear tests.

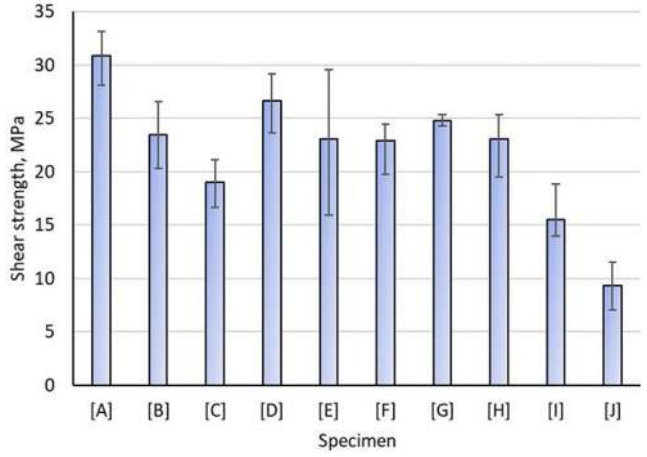

Fig. 11. Shear strength of each specimen in button shear tests.

- By combining microgrooves and LIPSSs with femtosecond laser treatment, micro- and nano-scale structures on the copper surface were successfully fabricated, and the adhesion strength between the copper and the EMC was improved by more than 3.3 times compared to that of the specimen without laser treatment. The LIPSS formation enhances the adhesion strength by approximately 7.3 % over that of the only microgroove structure.
- Depending on the position where the LIPSSs were formed, the adhesion strength changed, and the LIPSSs on the mountaintop showed the largest adhesion strength. The numerical simulation revealed that the LIPSSs suppressed the shear deformation of the EMC and worked as a resistance to the interface delamination, resulting in the enhancement of adhesion strength.

Based on the findings obtained in this study, combining micro- and nano-scale surface structure formations with femtosecond laser treatment is an effective method for improving adhesion strength.

Data availability

The raw/processed data required to reproduce these findings cannot be shared at this time due to technical or time limitations.

Data availability

Data will be made available on request.

Declaration of Competing Interest

The authors declare that they have no known competing financial interests or personal relationships that could have appeared to influence the work reported in this paper.

Acknowledgement

The authors thank Mr. Arita for his experimental support.

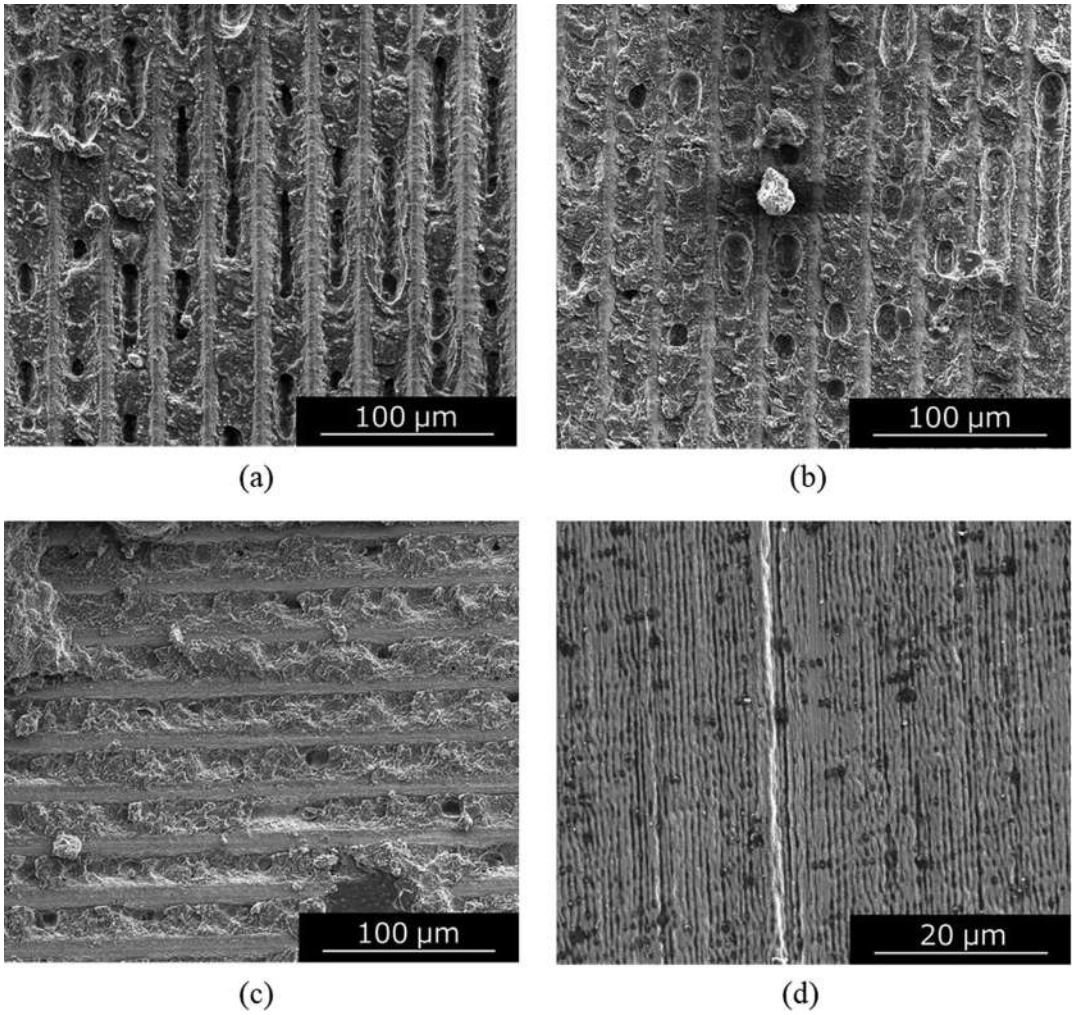

Fig. 12. (a) Fracture surface of specimen A (LIPSS: top, $d/2\lambda = 0.73$). (b) Fracture surface of specimen B (LIPSS: top, $d/2\lambda = 0.5$). (c) Fracture surface of specimen D (LIPSS: top and valley, $d/2\lambda = 0.47$). (d) Fracture surface of specimen I (only LIPSS).

References

[1] C. Bailey, Advances in Power Electronics, 2020 Pan Pacific Microelectronics Symposium (Pan Pacific), 2020. 10.23919/PanPacific48324.2020.9059348.

[2] B. Wang, J. Cai, X. Du, L. Zhou, Review of Power Semiconductor Device Reliability for Power Converters, CPSS Trans. Power Electron. Appl. 2(2) (2017) 101-117. 10.24295/CPSSTPEA.2017.00011.

[3] T. Kachi, D. Kikuta, T. Uesugi, Gan Power Device and Reliability for Automotive Applications, in: 2012 IEEE International Reliability Physics Symposium (IRPS), 2012, https://doi.org/10.1109/IRPS.2012.6241815.

[4] L. Guoyou, K. Li, Y. Wang, H. Luo, H. Luo, Recent Advances and Trend of HEV/EV-Oriented Power Semiconductors – an Overview, IET Power Electron. 13 (3) (2020) 394–404, https://doi.org/10.1049/iet-pel.2019.0401.

[5] A.J. Wileman, S. Aslam, S. Perinpanayagam, A Road Map for Reliable Power Electronics for More Electric Aircraft, *Prog. Aerospace Sci.* (2021/06/16/2021), 100739. 10.1016/j.paerosci.2021.100739.

[6] S. Xiong, Y. Guo, H. Yang, H. Zou, K. Wei, Reliability Study of Motor Controller in Electric Vehicle by the Approach of Fault Tree Analysis, *Eng. Failure Analy.* 121 (2021/03/01/ 2021) 105165. 10.1016/j.engfailanal.2020.105165.

[7] B. Mouawad, L. Yang, P. Agyakwa, M. Corfield, C.M. Johnson, Packaging Degradation Studies of High Temperature SiC MOSFET Discrete Packages, 2020 32nd International Symposium on Power Semiconductor Devices and ICs (ISPSD), 2020. 10.1109/ISPSD46842.2020.9170030.

[8] C. Lee, K. Kuo, C. Wang, J. Chang, W. Han, T. Chang, Packaging Reliability Estimation of High-Power Device Modules by Utilizing Silver Sintering Technology, *Microelectronics Reliability* 114 (2020/11/01/ 2020) 113890. 10.1016/j.microrel.2020.113890.

[9] G. Hu, R. Rossi, L. Jing-En, X. Baraton, Interface Delamination Analysis of TQFP Package During Solder Reflow, *Microelectron. Reliability* 50(7) (2010/07/01/ 2010) 1014-20. 10.1016/j.microrel.2010.03.012.

[10] H.T. Tran, M.H. Shirangi, X. Pang, A.A. Volinsky, Temperature, Moisture and Mode-Mixity Effects on Copper Leadframe/EMC Interfacial Fracture Toughness, Int. J. Fracture 185 (1) (2014) 115–127, https://doi.org/10.1007/s10704-013-9907-3.

[11] S. Swaminathan, K.S. Kamal, F.I. Richard, S. Tuhin, Measurement of Underfill Interfacial and Bulk Fracture Toughness in Flip-Chip packages, Microelectron. Reliability 66 (2016) 161–172, https://doi.org/10.1016/j.microrel.2016.09.008.

[12] K. Abhishek, D. Samet, V.N.N.T. Rambhatla, S.K. Sitaraman, Effect of Temperature and Humidity Conditioning on Copper Leadframe/Mold Compound Interfacial Delamination, Microelectron. Reliability 111 (2020) 113647, https://doi.org/10.1016/j.microrel.2020.113647.

[13] R.N. Wenzel, Resistance of Solid Surfaces to Wetting by Water, Ind. Eng. Chem. 28 (8) (1936) 988–994, https://doi.org/10.1021/ie50320a024.

[14] A.B.D. Cassie, S. Baxter, Wettability of Porous Surfaces, Trans. Faraday Soc. 40 (1944) 546–551, https://doi.org/10.1039/TF9444000546.

[15] Z. Yoshimitsu, A. Nakajima, T. Watanabe, K. Hashimoto, Effects of Surface Structure on the Hydrophobicity and Sliding Behavior of Water Droplets, Langmuir 18 (15) (2002) 5818–5822, https://doi.org/10.1021/la020088p.

[16] A. Marmur, Wetting on Hydrophobic Rough Surfaces: To Be Heterogeneous or Not to Be?, Langmuir 19 (20) (2003) 8343–8348, https://doiorg/10.1021/la0344682.

[17] T. Anish, W. Choi, M. Ma, J.M. Mabry, S.A. Mazzella, G.C. Rutledge, G.H. McKinley, R.E. Cohen, Designing Superoleophobic Surfaces, Science 318 (5856) (2007) 1618, https://doi.org/10.1126/science.1148326.

[18] T. Anish, W. Choi, G.H. McKinley, R.E. Cohen, M.F. Rubner, Design Parameters for Superhydrophobicity and Superoleophobicity, MRS Bull. 33 (8) (2008) 752–758, https://doi.org/10.1557/mrs2008.161.

[19] M. Nosonovsky, B. Bharat, Patterned Nonadhesive Surfaces: Superhydrophobicity and Wetting Regime Transitions, Langmuir 24 (4) (2008) 1525–1533, https://doi.org/10.1021/la702239w.

[20] M.C. Salvadori, M. Cattani, M.R.S. Oliveira, F.S. Teixeira, I.G. Brown, Design and Fabrication of Microcavity-Array Superhydrophobic Surfaces, J. Appl. Phys. 108 (2) (2010), https://doi.org/10.1063/1.3466979.
[21] M.C. Salvadori, M.R.S. Oliveira, R. Spirin, F.S. Teixeira, M. Cattani, I.G. Brown, Microcavity-Array Superhydrophobic Surfaces: Limits of the Model, J. Appl. Phys. 114 (17) (2013), https://doi.org/10.1063/1.4829003.
[22] S. Anjishnu, A. Kietzig, Design of a Robust Superhydrophobic Surface: Thermodynamic and Kinetic Analysis, Soft Matter 11 (10) (2015) 1998–2007, https://doi.org/10.1039/C4SM02787F.
[23] S. Yanlong, J. Zhao, Y. Fan, Z. Wan, L. Lu, Z. Zhang, W. Ming, L. Ren, Shape Memory Superhydrophobic Surface with Switchable Transition between "Lotus Effect" to "Rose Petal Effect", Chem. Eng. J. 382 (2020), https://doi.org/10.1016/j.cej.2019.122989.
[24] C. Greiner, A. del Campo, E. Arzt, Adhesion of Bioinspired Micropatterned Surfaces: Effects of Pillar Radius, Aspect Ratio, and Preload, Langmuir 23 (7) (2007) 3495–3502, https://doi.org/10.1021/la0633987.
[25] A.G. Peressadko, N. Hosoda, B.N.J. Persson, Influence of Surface Roughness on Adhesion between Elastic Bodies, Phys. Rev. Lett. 95 (12) (2005) 124301, https://doi.org/10.1103/PhysRevLett.95.124301.
[26] S.N. Ramakrishna, L.Y. Clasohm, A. Rao, N.D. Spencer, Controlling Adhesion Force by Means of Nanoscale Surface Roughness, Langmuir 27 (16) (2011) 9972–9978, https://doi.org/10.1021/la201727t.
[27] F.A. Cordisco, P.D. Zavattieri, L.G. Hector, B.E. Carlson, Mode I Fracture Along Adhesively Bonded Sinusoidal Interfaces, Int. J. Solids Struct. 83 (2016) 45–64, https://doi.org/10.1016/j.ijsolstr.2015.12.028.
[28] C.A. Fuentes, G. Brughmans, L.Q.N. Tran, C. Dupont-Gillain, I. Verpoest, A.W. Van Vuure, Mechanical Behaviour and Practical Adhesion at a Bamboo Composite Interface: Physical Adhesion and Mechanical Interlocking, Compos. Sci. Technol. 109 (2015) 40–47, https://doi.org/10.1016/j.compscitech.2015.01.013.
[29] A. Hamilton, Y. Xu, M.E. Kartal, N. Gadegaard, D.M. Mulvihill, Enhancing Strength and Toughness of Adhesive Joints Via Micro-Structured Mechanical Interlocking, Int. J. Adhesion Adhesives 105 (2021) 102775, https://doi.org/10.1016/j.ijadhadh.2020.102775.
[30] M. Kevin, N. Fleck, Tear Resistance of a Square-Wave Joint: Experiment Versus Cohesive Zone Model, Int. J. Adhes. Adhes. 84 (2018) 9–17, https://doi.org/10.1016/j.ijadhadh.2018.02.008.
[31] W. Kim, I. Yun, J. Lee, H. Jung, Evaluation of Mechanical Interlock Effect on Adhesion Strength of Polymer-Metal Interfaces Using Micro-Patterned Surface Topography, Int. J. Adhesion Adhesives 30 (6) (2010) 408–417, https://doi.org/10.1016/j.ijadhadh.2010.05.004.
[32] W. Zhang, L. Wei, H. Anmin, L. Ming, Adhesion Improvement of Cu-Based Substrate and Epoxy Molding Compound Interface by Hierarchical Structure Preparation, Microelectron. Reliability 52 (6) (2012) 1157–1164, https://doi.org/10.1016/j.microrel.2011.12.024.
[33] E.G. Baburaj, D. Starikov, J. Evans, G.A. Shafeev, A. Bensaoula, Enhancement of Adhesive Joint Strength by Laser Surface Modification, Int. J. Adhesion Adhesives 27 (4) (2007) 268–276, https://doi.org/10.1016/j.ijadhadh.2006.05.004.
[34] Y. Zhang, H. Yao, C. Ortiz, J. Xu, M. Dao, Bio-Inspired Interfacial Strengthening Strategy through Geometrically Interlocking Designs, J. Mech. Behav. Biomed. Mater. 15 (Nov 2012) 70–77, https://doi.org/10.1016/j.jmbbm.2012.07.006.
[35] I.A. Malik, M. Mirkhalaf, F. Barthelat, Bio-Inspired "Jigsaw"-Like Interlocking Sutures: Modeling, Optimization, 3D Printing and Testing, J. Mech. Phys. Solids 102 (2017) 224–238, https://doi.org/10.1016/j.jmps.2017.03.003.
[36] J. Long, P. Fan, M. Zhong, H. Zhang, Y. Xie, C. Lin, Superhydrophobic and colorful copper surfaces fabricated by picosecond laser induced periodic nanostructures, Appl. Surf. Sci. 311 (2014) 461–467, https://doi.org/10.1016/j.apsusc.2014.05.090.
[37] C. Chang, C. Cheng, J. Chen, Femtosecond laser-induced periodic surface structures of copper: Experimental and modeling comparison, Appl. Surf. Sci. 469 (2019) 904–910, https://doi.org/10.1016/j.apsusc.2018.11.059.
[38] R. Takase, S. Kodama, K. Shimada, H. Mescheder, K. Winands, J. Riepe, K. Arntz, M. Mizutani, T. Kuriyagawa, Study on the creation of Fine periodic structure on V-shaped groove with short-pulsed laser, Int. J. Autom. Technol. 14 (2020) 601–613, https://doi.org/10.20965/ijat.2020.p0601.
[39] S. Alamri, F. Fraggelakis, T. Kunze, B. Krupop, G. Mincuzzi, K. Kling, A.F. Lasagni, On the interplay of DLIP and LIPSS upon ultra-short laser pulse irradiation 1018(9 pages), Materials 12 (7) (2019), https://doi.org/10.3390/ma12071018.
[40] Q. Yao, J. Qu, Interfacial Versus Cohesive Failure on Polymer-Metal Interfaces in Electronic Packaging—Effects of Interface Roughness, J. Electron. Packag. 124 (2) (2002) 127–134, https://doi.org/10.1115/1.1459470.
[41] L.B. Freund, S. Suresh, Thin Film Materials: Stress, Defect formation and Surface evolution, Cambridge University Pres, 2003.
[42] T.L. Anderson, Fracture Mechanics: Fundamentals and Applications, third ed., CRC Press, 2005.
[43] L. Durix, M. Dreßler, D. Coutellier, B. Wunderle, On the Development of a Modified Button Shear Specimen to Characterize the Mixed Mode Delamination Toughness, Eng. Fracture Mech. 84 (2012) 25–40, https://doi.org/10.1016/j.engfracmech.2011.12.015.
[44] ABAQUS Documentation, 2021.
[45] H. Franz, K. Markus, Microscale simulation of adhesive and cohesive failure in rough interfaces, Eng. Fract. Mech. 178 (1) (2017) 416–432, https://doi.org/10.1016/j.engfracmech.2017.02.026.
[46] A. Nakajima, M. Omiya, J. Yan, Generation of micro/nano hybrid surface structures on copper by femtosecond pulsed laser irradiation, Nanomanuf. Metrol. 5 (2022) 274–282, https://doi.org/10.1007/s41871-022-00135-9.
[47] SEMI G69-0996, Test Method for Measurement of Adhesion Strength between Leadframes and Molding Compounds, SEMI, 1996.
[48] M. Goroll, R. Pufall, New Aspects in Characterization of Adhesion of Moulding Compounds on Different Surfaces by Using a Simple Button-Shear-Test Method for Lifetime Prediction of Power Devices, Microelectron. Reliab. 50 (9–11) (2010) 1684–2167, https://doi.org/10.1016/j.microrel.2010.07.038.
[49] P. Nadine, G.M. Reuther, M. Goroll, D. Udiljak, R. Pufall, B. Wunderle, Experimental Determination of Critical Adhesion Energies with the Advanced Button Shear Test, Microelectron. Reliab. 99 (2019) 177–185, https://doi.org/10.1016/j.microrel.2019.06.001.